Control of dynamic cell behaviors during angiogenesis and anastomosis by Rasip 1

Minkyoung Lee[1,3], Charles Betz[1], Ilkka Paatero[1,4], Niels Schellinx[1], Jianmin Yin[1], Christopher William Wilson[2,5], Weilan Ye[2], Markus Affolter[1,*] and Heinz-Georg Belting[1,*]

[1] Department of Cell Biology, Biozentrum, University of Basel, Klingelbergstrasse 70, 4056 Basel, Switzerland.

[2] Department of Molecular Biology, Genentech, Inc., South San Francisco, CA, USA.

[3] Current address: Department of Biosystems Science and Engineering, ETH Zurich, Mattenstrasse 26, 4058 Basel, Switzerland.

[4] Current address: Turku Centre for Biotechnology, University of Turku and Åbo Akademi University, Turku, 20520, Finland.

[5] Current address: Novartis Institutes for BioMedical Research, Cambridge, MA 02139, USA

[*]Correspondence: markus.affolter@unibas.ch (M.A.), heinz-georg.belting@unibas.ch (H.-G.B.)

Abstract

Organ morphogenesis is driven by a wealth of tightly orchestrated cellular behaviors, which ensure proper organ assembly and function. Many of these cell activities involve cell-cell interactions and remodeling of the F-actin cytoskeleton. Here, we analyze the requirement for Rasip1 (Ras-interacting protein 1), an endothelial-specific regulator of junctional dynamics, during blood vessel formation. Phenotype analysis of *rasip1* mutants in zebrafish embryos reveal distinct requirements for Rasip1 during sprouting angiogenesis, vascular anastomosis and lumen formation. During angiogenic sprouting, Rasip1 is required for efficient cell pairing, which is essential for multicellular tube formation. High-resolution time-lapse analyses show that these cell pairing defects are caused by a destabilization of tricellular junctions suggesting that tri-cellular junctions may serve as a counterfort to tether sprouting endothelial cells during morphogenetic cell rearrangements. During anastomosis, Rasip1 is required to establish a stable apical membrane compartment; *rasip1* mutants display ectopic, reticulated junctions and the apical compartment is frequently collapsed. Loss of Ccm1 and Heg1 function leads to junctional defects similar to those seen in *rasip1* mutants. Analysis of *radil-b* single and *rasip1/radil-b* double mutants reveal distinct and overlapping functions of both proteins. While Rasip1 and Radil-b have similar functions during angiogenic sprouting, the junction formation during anastomosis may primarily depend on Rasip1.

Keywords

Zebrafish, Endothelial cells, Angiogenesis, Anastomosis, VE-cadherin, Rasip1

44 # Introduction

45

46 The cardiovascular system is the first organ to become functional during embryonic
47 development. The generation of vascular networks is essential for developmental
48 patterning, growth and survival of the vertebrate embryo. As the embryo grows, the
49 vasculature adjusts to the increasing demand of nutrients and oxygen by an expansion
50 of the vasculature tree via sprouting angiogenesis, vascular remodeling and
51 adaptation of blood vessel diameter. Vascular morphogenesis is driven by a wealth of
52 dynamic cellular behaviors, which are regulated by molecular as well as physical cues,
53 and are characterized by an extraordinary plasticity (Adams and Alitalo, 2007;
54 Baeyens et al., 2016; Duran et al., 2017). At the cellular level, blood vessel
55 morphogenesis and remodeling are accomplished by endothelial cell behaviors
56 including cell migration, cell rearrangement and cell shape changes (Betz et al., 2016).
57 This repertoire of dynamic behaviors allows endothelial cells to rapidly respond to
58 different contextual cues, for example during angiogenic sprouting, anastomosis,
59 pruning, diapedesis or regeneration.
60 Previous studies have shown that vascular tube formation requires extensive and
61 diverse cell shape changes and that these changes can be driven by junctional
62 remodeling as well as dynamic regulation of the cortical actin cytoskeleton (Gebala et
63 al., 2016; Paatero et al., 2018; Phng et al., 2015; Sauteur et al., 2014). Junctional
64 remodeling is essential for cell rearrangements, which drive multicellular tube
65 formation. Enlargement of the luminal space, on the other hand, requires apical
66 membrane invagination (Barry et al., 2016; StriliC et al., 2009). During anastomosis,
67 the apical membrane can invaginate through the entire cell leading to the formation of
68 a unicellular tube (Lenard et al., 2013).

69 Junctional remodeling and membrane invagination rely on the dynamic regulation of
70 the F-actin cytoskeleton at the endothelial cell junction and apical cortex, respectively.
71 Small GTPases of the Rho family, including Cdc42, Rac1 and RhoA are essential
72 regulators of F-actin dynamics and have been shown to play critical roles during blood
73 vessel formation *in vitro* and *in vivo* (reviewed by (Barlow and Cleaver, 2019). In the
74 vasculature, these GTPases are partially regulated by the adaptor protein Rasip1.
75 Rasip1 has been shown to promote Rac1 and Cdc42 activity, whereas it inhibits RhoA
76 activity by binding to the GTPase activating protein Arhgap29 (Barry et al., 2016; Xu
77 et al., 2011). Ablation of Rasip1 in mice and knock-down of *rasip1* zebrafish cause
78 severe vascular defects (Wilson et al., 2013; Xu et al., 2011). During vasculogenesis,
79 Rasip1 is required for the lumenization of the dorsal aorta, in particular for the clearing
80 of apical membrane compartments from junctional proteins and for the opening of the
81 vascular lumen between endothelial cells (Barry et al., 2016). However, the role of
82 Rasip1 during sprouting angiogenesis and anastomosis has not been studied in detail.
83 To gain more insight into the cellular and molecular mechanisms of vascular tube
84 formation during angiogenesis, we have generated loss-of-function alleles in the
85 zebrafish *rasip1* gene and performed high-resolution time-lapse imaging to observe
86 junctional dynamics during sprouting angiogenesis and anastomosis. Loss of *rasip1*
87 causes multiple vascular defects, with respect to angiogenic sprouting, including
88 defects in cell proliferation, junctional stability and lumen formation. Furthermore,
89 analyses of *radil-b* and *rasip1;radilb* double mutants reveal partly redundant roles for
90 the two proteins. Lastly, knock-down of *ccm1* and *heg1* phenocopies the apical
91 junctional defects seen in *rasip1*, suggesting a functional interaction between the
92 proteins during blood vessel formation.

93 # Results

94

95 **Loss of Rasip1 function causes broad vascular defects**

96 To investigate the role of Rasip1 in vascular morphogenesis we employed
97 CRISPR/Cas9 technology to generate several mutant alleles, namely *rasip1*^{ubs23},
98 *rasip1*^{ubs24} and *rasip1*^{ubs28}, respectively (S-Figure 1). The *rasip1*^{ubs28} allele comprises
99 a deletion of about 35kb including the *rasip1* coding region from exon 3 to 16, encoding
100 a severely truncated protein lacking the Ras-association, Forkhead-association and
101 Dilute domains (Figure 1a). Since the truncated protein lacks all the conserved
102 domains, we consider *rasip1*^{ubs28} to be a null-allele and focused our studies on the
103 analysis of this mutant.

104 Homozygous *rasip1* mutants displayed hemorrhages and vascular instability in the
105 cranial vasculature at 3 days of development (Figure 1b,c). Furthermore, we observed
106 transient pericardial edema between 3 and 5 dpf (Figure 1d), which usually
107 disappeared during larval development. In the trunk, *rasip1* mutants showed reduced
108 blood flow, which correlated with irregular and generally reduced diameter of the
109 dorsal aorta (DA) and intersegmental vessels (ISVs) (Figure 1e-g). These differences
110 were transient and by 5 dpf the average vessel diameter had recovered to normal size.
111 Despite these severe defects, homozygous *rasip1* mutants recovered and about 30%
112 of them developed to fertility.

113

114 **Reduced motility and proliferation during angiogenic sprouting in *rasip1***
115 **mutants**

116 To find out whether the loss of *rasip1* may affect dynamic cell behaviors, we performed
117 time-lapse analyses, concentrating on the developing ISVs. ISVs sprouts emerge from

118 the DA at about 22-24 hpf and extend towards the dorsal side of the embryo. In wild-
119 type embryos, they reach the dorsal part of the neural tube by 28 hpf and initiate
120 formation of the dorsal longitudinal anastomotic vessel (DLAV) (Lawson and
121 Weinstein, 2002). In our time-lapse movies we observed that by 30 hpf almost all
122 sprouts in the trunk region had completed dorsal sprouting and engaged in contact
123 with neighboring sprouts (S-Figure 2a, b). In contrast, ISV sprouting in *rasip1* mutants
124 appeared sluggish and 25% of sprouts were incomplete by 30 hpf (S-Figure 2a,b). To
125 see whether stunted outgrowth was reflected by a difference in the number of
126 endothelial cells contributing to ISV sprouts, we counted nuclei within each sprout at
127 30 hpf (S-Figure 2c). In wild-type and *rasip1* mutants, the number ISV nuclei was quite
128 variable ranging between one and five. However, we observed a clear enrichment of
129 ISVs containing one or two nuclei in mutants when compared to wild-type, which
130 contained three to four nuclei. To differentiate whether this diminished cell number
131 was caused either by reduced recruitment or by proliferation defects of endothelial
132 cells, we tracked endothelial cell nuclei during ISV formation (S-Figure 2d-g). In wild-
133 type siblings, we observed that two cells migrated from the DA into the sprout,
134 undergoing one round of division each thus giving rise to an ISV consisting of four
135 cells (S-Figure 2e); ISVs comprising three cells were usually formed by two migrating
136 cells and a single cell division (S-Figure 2f). In *rasip1* mutants we rarely observed cell
137 divisions within the sprouts (S-Figure 2d,g). Instead, most cells in the sprout originated
138 from the DA and occasionally we observed three cells migrating into the sprout (Figure
139 2f). Hence, these results show that proliferation in sprouting endothelial cells is
140 reduced in *rasip1* mutants and suggest that paucity of cell number may partially be
141 compensated by the recruitment of additional cells into the sprout.
142

143 **Instability of tricellular junctions inhibits formation of multicellular tubes**

144 We next examined whether loss of *rasip1* affects angiogenic tube formation. In wild-
145 type embryos, the multicellular architecture of ISVs tubes is established via concerted
146 migratory and proliferative activities of endothelial cells. More specifically, the
147 multicellular configuration is driven by junctional rearrangements along the vessel axis,
148 which leads to effective cell pairing and thus multicellularity.

149 Since multicellular tubes are characterized and can be recognized by continuous
150 junctions along the blood vessel axis (Blum et al., 2008), we used a *ve-cad:ve-cad-*
151 *Venus* reporter (Lagendijk et al., 2017) to follow the dynamics of endothelial junctions
152 during ISV formation. In wild-type siblings, cell junctions elongated and spanned the
153 entire extend of the ISV giving rise to multicellular tubes by 48 hpf (Figure 2a,b,f).
154 Notably, adherens junctions maintained the continuity of the ISVs with the DA, where
155 they formed vertices or tri-cellular junctions (Figure 2a, white arrowheads). *rasip1*
156 mutants showed a clear delay in multicellular tube formation (Figure 2c) and at 48 hpf
157 – on average – about 40% of ISVs had not achieved a multicellular configuration
158 (Figure 2b). Moreover, time-lapse analysis of VE-cad-Venus showed defects in
159 junctional development (Figure 2a). Specifically, at the ventral base of the sprout,
160 junctions that were normally tethered to the DA in wild-type embryos, lost this
161 attachment and the junctional ring was "released" in mutant embryos (Figure 2a,
162 yellow arrowheads,d). This detachment resulted in one of the stalk cells moving up
163 into the DLAV leaving a single cell spanning the distance between the DA and the
164 DLAV (Figure 2a,e,f). These results indicate that junctional interconnections at the
165 base of the sprout are critical for cell intercalation to occur during multicellular tube
166 formation. Thus, the loss of these connections in *rasip1* mutant prevents cell pairing

167 and results in unicellular ISVs and consequently a defect in the cord hollowing process
168 underlying multicellular tube formation.
169
170 **Defects in junctional dynamics during blood vessel anastomosis**
171 The growth and interconnection of vascular networks requires angiogenic sprouting
172 as well as the interconnection of all sprout by the process of anastomosis. At the
173 cellular level, anastomosis occurs in a quite stereotyped fashion (reviewed by (Betz et
174 al., 2016). Neighboring sprouts initiate contact via tip cell filopodia and form a
175 junctional ring which surrounds apically polarized membrane. Junctional ring and
176 apical membrane formation in both of the contacting cells leads to the formation of a
177 luminal pocket, which is later connected to the lumen of the nascent vessel. The
178 process of anastomosis in zebrafish serves as a paradigm to study the cell biology of
179 blood vessel formation and includes processes such as apical polarization, junctional
180 rearrangements and lumen formation, which occur within a 4 to 6 hours (Herwig et al.,
181 2011). To assess the role of Rasip1 during anastomosis, we compared the dynamics
182 of junctional reporters such as VE-cad-Venus (Figure 3a) and Pecam-EGFP (S-Figure
183 3) in wild-type and mutant embryos. Time-lapse analyses revealed two different
184 defects in *rasip1* mutants during junctional ring formation. In about 53% of
185 anastomosis events (Figure 3a) we observed ectopic accumulation of VE-cadherin-
186 Venus or Pecam-EGFP (S-Figure 3) within the junctional ring, revealing a defect in
187 relocating these junctional proteins from the apical compartment to cell junctions.
188 Alternatively, in about 34% of cases, the anastomotic ring (Figure 3c,e,f) elongated
189 along the blood vessel axis but failed to maintain a lateral axis, leading to a collapsed
190 junctional ring.
191

192

193 The described defects were confirmed by immunofluorescent analysis of the junctional
194 proteins VE-cad, ZO-1 (tight junction protein 1, Tjp1) and Esama (endothelial-selective
195 adhesion molecule a) (Figure 3d-e). In *rasip1* mutants VE-cad, Zo-1 as well as Esama
196 colocalized and formed reticulated junctions within the apical compartment. Together,
197 these observations indicate that Rasip1 plays a crucial role in the dynamic re-
198 localization of junctional components during *de novo* junction and lumen formation.

199

200 ***rasip1* mutants display transient intracellular luminal pockets**

201 As shown above *rasip1* mutant embryos display reduced vessel diameter and luminal
202 defects (Figure 1e-g). These luminal defects affect the onset of blood flow in the ISVs
203 (Figure 4a, yellow arrowhead). We observed that initially unlumenized ISVs remained
204 unlumenized at least through day 4 of development (96 hpf) (Figure 4b). Moreover, in
205 some instances we observed that initially lumenized blood carrying ISVs collapsed in
206 subsequent stages (up to 96 hpf), indicating a role for Rasip1 in lumen maintenance
207 (Figure 4b,c). Thus, although luminal defects can be attributed to the inability of
208 endothelial cells to rearrange into a multicellular configuration (Figures 2 and 3), the
209 above observations suggest an additional defect in the formation or maintenance of a
210 continuous luminal compartment. This notion is supported by time-lapse analysis of
211 ISV and DLAV formation during lumen formation (Figure 5a). The timing of lumen
212 formation in the ISV is variable but usually starts between 30 and 32 hpf. In wild-type
213 embryos we observed that upon initiation, continuous lumens were formed within 30
214 minutes (Figure 5a). In *rasip1* mutants, lumen formation was delayed and
215 discontinuous. Instead, we often observed luminal pockets in the dorsal aspects of the
216 ISV (Figure 5a, yellow arrowheads, S-Figure 5d). We surmised that luminal pockets

217 could arise in three different ways (Figure 5b) – either (1) by a collapse of a previously
218 patent tube, (2) by a local cord hollowing event, which failed to interconnect with other
219 luminal pockets or (3) by the formation of large intracellular vacuolar structures, which
220 failed to fuse with luminal membrane.
221 To differentiate between these scenarios, we performed a series of experiments. To
222 test whether luminal pockets may arise by lumen collapse, we performed
223 microangiography using a fluorescent tracer dye in 28 to 30 hpf embryos (Figure 5c).
224 Upon intravascular injection, the entire patent vasculature was labelled by quantum
225 dots. In *rasip1* mutants, however, we observed that although the base of the ISV was
226 positive for quantum dots, local luminal pockets in the DLAV were negative (Figure 5c,
227 yellow arrowheads). This strongly argues that luminal pockets in *rasip1* mutants arise
228 locally and do not represent luminal remainders formed by lumen collapse.
229 We next wanted to check whether luminal pockets represented intra- or extracellular
230 compartments. Extracellular luminal compartments arise between cells in a process
231 called cord hollowing, whereas intracellular lumens are thought to form by vacuolation
232 (Davis et al., 2011). During anastomosis in zebrafish embryos, cord hollowing
233 generates luminal pockets form as transient structures at the interface between
234 contacting tip cells (Blum et al., 2008). This interface is formed by a ring-shaped
235 junction, which surrounds an apical compartment of both tip cells (Herwig et al., 2011).
236 Thus, these extracellular pockets are demarcated by junctional rings, while
237 intracellular pockets should be outside of these rings. To test these possibilities, we
238 examined lumen formation in *rasip1* mutants expressing VE-cad-Venus and found that
239 they were located outside the junctional ring (Figure 5d (00:12)), appearing as
240 vesicular structures within the endothelial cytoplasm. Lateron (Figure 5d (01:32)) these
241 intracellular lumens were incorporated into the area covered by the junctional ring,

242 therefore representing transient structures. Taken together, these findings show that
243 loss of Rasip1 function leads to a transient accumulation of intracellular vesicles, which
244 later on merge into the anastomotic compartment suggesting that Rasip1 may be
245 critical for normal vesicle transport or vesicle fusion during cord hollowing process,
246 which occurs during anastomosis.
247
248 **Rasip1 localizes to apical membranes and endothelial cell junctions**
249 Our mutant analyses indicate a requirement for Rasip1 in junction formation and
250 remodeling, as well as in lumen formation and maintenance. To gain a better
251 understanding of how Rasip1 may be involved in these processes, we generated an
252 antibody against zebrafish Rasip1 to discern the subcellular localization of the protein
253 during angiogenesis. Immunofluorescent analysis confirmed endothelial expression of
254 Rasip1 in zebrafish embryos (S-Figure 4). Notably, Rasip1 protein levels appeared
255 dynamically regulated. During vasculogenesis, until the emergence of intersegmental
256 sprouts, Rasip1 was detected at high levels in the dorsal aorta (S-Figure 4a,b, yellow
257 arrowheads). In contrast, Rasip1 protein was highly expressed in sprouting ISVs while
258 it became downregulated in the dorsal aorta (S-Figure 4c, yellow bars), supporting the
259 notion that Rasip1 primarily functions during blood vessel morphogenesis rather than
260 during vessel maintenance. High-resolution imaging revealed specific subcellular
261 localization during blood vessel formation. In the context of anastomosis, three
262 different phases could be discerned. First, during contact formation (30 hpf), we found
263 that Rasip1 is absent from newly formed contacts (Figure 6a, yellow arrowheads).
264 However, Rasip1 was observed colocalizing with large junctional patches prior to
265 discernable formation of apical compartments. During later stages of anastomosis,
266 when the anastomotic ring had formed, Rasip1 was restricted to the apical

267 compartment within the junctional ring with no detectable Rasip1 at the junction
268 (Figure 6b, yellow arrowheads). However, shortly later - during the establishment of
269 the DLAV (36 hpf) and later after full development of angiogenic vessels (48 hpf) - ,
270 we found that Rasip1 also localized to endothelial cell junctions (Figure 6c, white
271 arrowheads). Taken together, these studies show that Rasip1 dynamically distributes
272 during different phases of blood vessel formation. In particular, the dynamic subcellular
273 distribution to apical membrane compartments and endothelial cell junctions suggests
274 a sequential requirement for Rasip1 during apical compartment formation and
275 junctional remodeling, respectively.
276
277 Because of the early localization of Rasip1 to the apical membrane, we wanted to test
278 whether loss of Rasip1 function may affect apical polarization during blood vessel
279 formation. To this end, we generated a transgenic reporter (*Tg(EGFP-podxl)*^{ubs29}),
280 which labels the apical membrane compartment (S-Figure 5a). At 48 hpf, we observed
281 normal luminal localization of EGFP-Podxl in *rasip1* mutants (S-Figure 5b). In ISVs
282 that displayed luminal defects, we observed slightly irregular distribution of EGFP-
283 Podxl in affected areas (enlarged insets in S-Figure 5b). These observations suggest
284 that in spite of its apical localization, Rasip1 is not required for apical polarization in
285 endothelial cells.
286
287 **Overlapping requirement of Rasip1 and Radil-b in blood vessel formation**
288 Rasip1 protein has been shown to be an effector protein of the small GTPase Rap1
289 (Gingras et al., 2016). Protein binding studies have shown that Rasip1 can form
290 multimeric complexes consisting of Rap1, Rasip1, Radil (Ras-associating-dilute-
291 domain) and the GTPase-activating protein Arhgap29 (Post et al., 2013). Furthermore,

292 it has been shown that the core of these complexes can be formed by a Rasip1
293 homodimer or a Rasip1/Radil heterodimer (de Kreuk et al., 2016), indicating partly
294 overlapping functions of these proteins in endothelial cells. Rasip1 and Radil are
295 closely related proteins (S-Figure 6a) sharing several protein interaction domains such
296 as a Ras association (RA) domain conferring binding to Rap1, and a forkhead
297 association (FHA) domain binding the transmembrane receptor Heg1. An additional
298 PDZ domain is unique to Radil and is thought to interact with the GTPase-activating
299 protein Arhgap29 (Post et al., 2013). Radil function in endothelial cells has, so far, only
300 been addressed in cell culture experiments, which established its above-mentioned
301 protein interactions and indicated a role of Radil in endothelial barrier maintenance
302 and the regulation of endothelial cell adhesion (de Kreuk et al., 2016; Pannekoek et
303 al., 2014). Thus, we wanted to determine the role of Radil during blood vessel
304 morphogenesis *in vivo* and compare its requirement to that of Rasip1. The zebrafish
305 genome contains three *radil* paralogues, *radil-a,-b* and *-c*, respectively (S-Figure 6a).
306 Whole-mount in situ analysis revealed that of the three paralogues, only *radil-b* was
307 expressed specifically in endothelial cells (data not shown). Therefore, we analyzed
308 blood vessel formation in *radilb*^{sa20161} mutants, which carry a nonsense mutation
309 (Tyr129 → STOP) near the N-terminus of the protein (S-Figure 6b).
310 *radil-b* mutants were homozygous viable and could be raised to fertility. Nevertheless,
311 they exhibited several vascular defects similar to *rasip1* mutants, including cerebral
312 hemorrhages (S-Figure 6c), isolated luminal pockets (S-Figure 6d), reduction of blood
313 flow (S-Figure 6e) and retarded sprouting of ISVs (data not shown), supporting the
314 notion that both proteins are involved in the same molecular pathways. In contrast,
315 *radil-b* mutants did not phenocopy the junctional re-localization defect observed in
316 *rasip1* mutants during anastomosis (Figure 7a), suggesting that the proteins may also

317 have unique functions. *radil-b* mutants generally exhibited milder defects (S-Figure 6f,
318 g), in particular with respect to cellular architecture compared to single *rasip1* mutants
319 and *rasip1;radil-b* double mutants (Figure 7b). Furthermore, *rasip1;radil-b* double
320 mutants showed stronger sprouting and lumen formation defects than either single
321 mutant (Figure 7, S-Figure 6h), suggesting that while both proteins are required in this
322 process, they likely act in a partially redundant manner.
323
324 **Knock-down of *ccm1* and *heg1* phenocopies aspects of the *rasip1* mutant**
325 The Rasip1/Radil/Rap1 complex can bind via the FHA domain to the orphan
326 transmembrane receptor Heg1 (Gingras et al., 2016). This interaction has been shown
327 to tether Rasip1 to endothelial cell junctions (Post et al., 2013). To address the
328 relevance of this interaction during ISV morphogenesis, we analyzed *heg1* morphants
329 in order to test whether loss of Heg1 function showed any *rasip1*-like vascular
330 phenotypes. We also examined the phenotypes of *ccm1* morphants. Ccm1 binds to
331 Heg1 independently of Rasip1 (Gingras et al., 2012), and thus might indirectly
332 influence Rasip1 function. *ccm1* and *heg1* morphants exhibited blood vessel and heart
333 dilations as previously published (S-Figure 7a) (Hogan et al., 2008; Kleaveland et al.,
334 2009; Stainier et al., 1996). We consistently observed hemorrhages, which were less
335 pronounced than in *rasip1* mutants (Figure 8a and S-Figure 7b). However, similar to
336 *rasip1* mutants, ISV sprouting and development appeared to be delayed (Figure 8b).
337 To assess the role of Heg1 and Ccm1 in junctional rearrangements, we analyzed
338 endothelial cell junctions in transgenic VE-cad-Venus and Pecam1-EGFP reporter
339 background (S-Figure 7e). Consistent with earlier reports (Hogan et al., 2008;
340 Kleaveland et al., 2009), knock-down of *ccm1* or *heg1* did not cause obvious junctional
341 defects in the dorsal aorta. However, we observed detachment of junctions and

342 impaired cell rearrangements in sprouting ISVs (S-Figure 7c, d). In addition, it
343 appeared that Pecam-EGFP as well as VE-cad-Venus were not entirely cleared from
344 apical compartments during the formation of the DLAV.
345 To verify these observations, we performed immunofluorescent analyses to determine
346 whether endogenous VE-cadherin protein was cleared from the apical membrane
347 compartment in *heg1* and *ccm1* morphants. In both conditions, VE-cadherin
348 accumulated in the apical compartment embedded within the junctional rings – similar
349 to what we observed of *rasip1* mutants (Figure 8c). *In vivo* imaging of the junctions in
350 *ccm1* or *heg1* knock-down embryos showed a failure of multicellular vessel formation
351 (Figure 8d). Taken together, these findings show that *ccm1* and *heg1* loss-of-function
352 phenocopy defined aspects of *rasip1* mutants during critical aspects of blood vessel
353 formation during sprouting angiogenesis and anastomosis.
354

355 ## Discussion

356 Small GTPases of the Rho family play a key role in the regulation of cellular activities
357 during blood vessel formation. For example, they serve as molecular switches to
358 control cytoskeletal dynamics, cell adhesion and junction assembly during angiogenic
359 sprouting and lumen formation (Barlow and Cleaver, 2019). Rasip1 has been
360 described as an effector protein of small GTPase signaling during blood vessel
361 formation and maintenance (Koo et al., 2016; Wilson et al., 2013; Xu et al., 2011).
362 Rasip1 protein contains multiple protein binding domains and has been shown to
363 directly interact with its paralogue Radil, the small GTPase Rap1 and the
364 transmembrane protein Heg1 (de Kreuk et al., 2016; Gingras et al., 2016; Wilson et
365 al., 2013). By further association with proteins such as Arhgap29 and Ccm1, these
366 proteins control cortical actomyosin tension and endothelial junction formation and

367 dynamics (Post et al., 2015) and reviewed by (Lampugnani et al., 2017; Wilson and
368 Ye, 2014). Analyses of mutant mouse embryos have shown that Rasip1 is required
369 for proper lumen formation and maintenance in blood and lymphatic vessels (Koo et
370 al., 2016; Liu et al., 2018; Wilson et al., 2013). During vasculogenesis, Rasip1 is
371 required for the establishment of the nascent apical compartment and subsequently
372 for lumen expansion, presumably mediated by regulating Cdc42 and RhoA,
373 respectively (Barry et al., 2016).
374
375 **Multiple vascular defects in zebrafish *rasip1* mutants**
376 In order to gain a better understanding of how morphogenetic cell behaviors are
377 controlled by Rasip1, we generated loss-of-function mutants in the zebrafish *rasip1*
378 gene and analyzed these mutants focusing on cellular and junctional dynamics during
379 angiogenic sprouting and anastomosis. Overall, our findings are in agreement with
380 previously published vascular defects in mouse development, but also provide novel
381 insights into the regulation of junctional dynamics during angiogenic sprouting and
382 lumen formation.
383 *rasip1* mutants display numerous vascular defects, including cranial hemorrhage,
384 reduced blood circulation and reduced diameter of the dorsal aorta, consistent with
385 previously published *rasip1* knockdown experiments in zebrafish (Wilson et al., 2013).
386 Furthermore, we observe delayed angiogenic sprouting, as well as abnormalities in
387 lumen formation as well as impaired cell rearrangements, junctional dynamics and
388 stability. Despite this wide range of defects, the mutant phenotypes are consistent with
389 defects in the control of F-actin and junctional dynamics. The phenotypes of *rasip1*
390 mutants during vascular development are, however, quite distinct from those seen in

391 *ve-cad (cdh5)* mutants (Sauteur et al., 2014) indicating that Rasip1 is regulating
392 endothelial activities beyond cell junctions.
393
394 **Dynamic regulation of Rasip1 expression and subcellular localization**
395 Endothelial-specific expression of Rasip1 has been reported in several vertebrate
396 species including mouse, *Xenopus* and zebrafish, and Rasip1 appears to be
397 expressed in the entire embryonic vasculature (Wilson et al., 2013; Xu et al., 2009). In
398 contrast to its broad endothelial transcription, the distribution of Rasip1 protein
399 appears to highly regulated, with respect to the overall level and its subcellular
400 localization. During vasculogenesis, Rasip1 is readily detected at high levels in the
401 dorsal aorta, whereas at later stages expression is somewhat reduced. This
402 downregulation of Rasip1 in the dorsal aorta coincides with the commencement of
403 blood flow, suggesting that Rasip1 protein levels and localization may be controlled by
404 shear stress. The downregulation of Rasip1 protein in more mature vessels suggests
405 an essential role during blood vessel morphogenesis. In agreement with this, Rasip1
406 does not appear to be required in established blood or lymphatic vessels (Koo et al.,
407 2016; Liu et al., 2018).
408 During ISV sprouting we observe a shift of Rasip1 from the apical membrane
409 compartment during the early stages to higher levels at cell junctions during the later
410 stages of vascular tube formation. The early apical localization of Rasip1 is in
411 agreement with a previously proposed role in early apical-basal polarization, likely
412 upstream of Cdc42 (Barry et al., 2016). It will be important to determine how this
413 differential localization is accomplished or to what extend it reflects different functions
414 of Rasip1 during tubulogenesis. In *Drosophila*, it has been shown that apical
415 localization of canoe (the ortholog of vertebrate *afadin* and a homologue of rasip1) is

416 dependent on Rap1 (Bonello et al., 2018). Therefore, Rap1 is a putative candidate to
417 localize Rasip1 to apical membrane during vertebrate angiogenesis.
418
419 **A role for Rasip1 in angiogenic sprouting and blood vessel assembly**
420 Sprouting angiogenesis is accomplished by concerted endothelial cell dynamics
421 including cell migration, rearrangement, elongation and proliferation, all of which are
422 affected by the loss Rasip1 function. *rasip1* mutant ISVs contain fewer cells than wild-
423 type ISV, which reflects a reduced rate of cell proliferation during sprouting.
424 Furthermore, we observe a frequent failure of *rasip1* mutant ISVs to form multicellular
425 tubes. Formation of multicellular ISVs does not depend of the number of cells present
426 in the sprout (Angulo-Urarte et al., 2018) but rather relies on cell rearrangements
427 driven by junctional remodeling (Sauteur et al., 2014). For example, loss of VE-cad
428 prevents junction elongation and renders endothelial cells unable to move over each
429 other and effectively pair to form a multicellular tube (Paatero et al., 2018; Sauteur et
430 al., 2014). In *rasip1* mutants, however, the defect in cell pairing is caused by junctional
431 detachments. When we imaged VE-cad dynamics during ISV sprouting in wild-type
432 embryos, we found that, in many cases, two stalk cells maintain contact to the dorsal
433 aorta. In *rasip1* mutant sprouts, we observed that one of these cells detached from the
434 dorsal aorta and “retracted” to the dorsal part of the ISV, leaving the remaining cell
435 unpaired. Stalk cell detachment appears to occur at tri-cellular junctions indicating that
436 these junctions may be important as an anchor point to resist mechanical forces
437 occuring during cell rearrangements. A study performed in MDCK cells has shown that
438 Afadin accumulates at tri-cellular junctions in response to tension (Choi et al., 2016).
439 This finding supports the interesting notion that Rasip1 may play a specific role in
440 reinforcing tri-cellular junctions during sprouting angiogenesis.

441

442 **Rasip1 is required for lumen patency**

443 Lumen formation in *rasip1* mutants is delayed and ISVs as well as the dorsal aorta
444 show reduced vessel diameters during early embryonic development. At 48 hpf, we
445 observed that about 50% of the ISVs were not patent and this defect was maintained
446 at least through day 4 of development. Defects in luminal patency may have multiple
447 causes. First, as described above, junctional detachment can prevent endothelial cell
448 pairing and thus multicellular tube formation. Second, our examinations of the apical
449 membrane using a Podxl-EGFP and Cherry-CAAX transgenic markers revealed an
450 irregular shape of the apical membrane, suggesting luminal collapse. This observation
451 agrees with earlier findings that Rasip1 regulates cortical actin tension during lumen
452 opening of the dorsal aorta in mouse (Barry et al., 2016).
453 During the formation of the DLAV formation, we also observed luminal pockets, which
454 did not label by microangiography and appeared outside of cell junctions, indicating
455 that these lumens are intracellular and consist of large vesicles or vacuolar structures.
456 Rasip1 has been shown to associate with early Rab5-positive and recycling Rab8-
457 positive endosomes (Barry et al., 2016) and Rab8 has been implicated in the transport
458 of Podocalyxin to the apical membrane in a Cdc42 dependent manner (Bryant et al.,
459 2010). Further analyses will have to be undertaken to determine whether these
460 intracellular lumens are endosomal compartments and whether Rasip1 plays a role in
461 targeting recycling endosomes to the apical compartment.

462

463 **Rasip1 during anastomosis**

464 Vascular anastomosis is the process by which blood vessel connect and form a
465 network. Formation of the DLAV in the zebrafish is initiated by the interaction of two

466 neighboring tip cells which establish contact and form a localized *de novo* lumen at
467 their interface (Herwig et al., 2011) reviewed by (Betz et al., 2016). Formation of this
468 luminal pocket follows a relatively stereotyped sequence: upon initial interfilopodial
469 contact a junctional spot is formed, which is transformed into a ring surrounding apical
470 membrane. This spot to ring transformation entails the formation and expansion of a
471 stable junctional ring and the removal of junctional proteins from the center to permit
472 formation of an apical membrane compartment. Loss of Rasip1 prevents apical
473 clearance leading to ectopic junctions within newly formed apical compartments. A
474 similar phenotype has been observed in *Rasip1* mouse mutants during lumen
475 formation of the dorsal aorta and it was shown that this requirement is upstream of
476 Cdc42 (Barry et al., 2016). Thus, the molecular mechanisms driving apical clearance
477 during vasculogenesis and anastomosis appear to be rather conserved.
478 *In vitro* experiments have shown that Rasip1 localization at cell junctions requires its
479 interaction with the orphan receptor Heg1 (de Kreuk et al., 2016) and it has been
480 suggested that Rasip1 acts in concert with Heg1, Rap1 and Ccm1 and other proteins
481 in junction stabilization (reviewed by (Lampugnani et al., 2017)). To test whether
482 Rasip1, Ccm1 and Heg1 may interact during apical clearance, we performed
483 knockdown experiments. Knockdown of *ccm1* as well as *heg1* in zebrafish phenocopy
484 the apical clearance defects seen in *rasip1* mutants. Taken together, these data
485 suggest that some of the pathways which are involved in junction stabilization are also
486 required for or result in apical clearance during *de novo* lumen formation.
487 Rasip1, Radil and Arghap29 have been shown to form a complex and are thought to
488 regulate RhoA. Our analysis of *radil-b* and *rasip1/radil-b* double mutants has shown
489 that both proteins have similar functions during angiogenic sprouting and lumen
490 formation and maintenance. However, Radil-b appears to be dispensable for apical

491 junctional re-localization during anastomosis. In agreement with this interpretation,
492 studies in the mouse dorsal aorta have shown that clearance of apical junction
493 requires Cdc42 and is independent of RhoA (Barry et al., 2016).
494 In mouse dorsal aortae, loss of Rasip1 leads to an overactivation of Rock and an
495 increase of cortical actomyosin tension in the apical compartment (Barry et al., 2016).
496 As a consequence, the luminal surface of the endothelium cannot expand and the
497 lumen is constricted. In relation to this, we observe a collapse of the junctional ring
498 during anastomosis while the junctions are still maintained and elongate along the
499 vascular axis, resulting in a narrower apical compartment within the ring, eventually
500 leading to a close alignment of the junctions along the extending axis. We speculate
501 that this collapse of the junctional ring may be caused by an imbalance of the cortical
502 actin between apical and basolateral compartment, caused by an overactivation of
503 Rock at the apical side. Further studies on local actomyosin regulation will be required
504 to better understand the formation of a luminal surface during vasculogenesis and
505 vascular anastomosis.
506

507 # Materials and Methods

508 **Zebrafish Strains and Morpholinos**

509 Zebrafish were maintained according to FELASA guidelines (Aleström et al., 2019).
510 All experiments were performed in accordance with federal guidelines and were
511 approved by the Kantonales Veterinäramt of Kanton Basel-Stadt. Zebrafish lines used
512 were *Tg(gata1a:DsRed)*^{sd2} (Traver et al., 2003), *Tg(kdrl:EGFP)*^{s843} (Jin, 2005),
513 *Tg(kdrl:EGFPnls)*^{ubs1} (Blum et al., 2008), *Tg(5xUAS:RFP)* (Asakawa and Kawakami,
514 2008), *Tg(fli1ep:gal4ff)*^{ubs3} (Herwig et al., 2011), *Tg(fli1a:Pecam-EGFP)*^{ncv27} (Ando et
515 al., 2016), *Tg(cdh5:cdh5-TFP-TENS-Venus)*^{uq11bh} (Lagendijk et al., 2017),
516 *Tg(UAS:EGFPpodxl)*^{ubs29} (this study) and *rasip1*^{ubs28} (this study) and *radilb*^{sa20161}
517 (European Zebrafish Resource Center, Karlsruhe, Germany). Morpholinos (Gene-
518 Tools, Corvallis, OR, USA) used were as follows:
519 *ccm1* 5'-GCTTTATTTCACCTCACCTCATAGG-3' (Mably, 2006),
520 *heg1* 5'-GTAATCGTACTTGCAGCAGGTGACA-3' (Mably et al., 2003),
521 standard control 5'-CCTCTTACCTCAGTTACAATTTATA-3'.
522

523 **Generation of *Tg(UAS:EGFPpodxl)*^{ubs29}**

524 The p5E-4xnrUAS promoter, pME-EGFP-podocalyxin (Navis et al., 2013) and p3E-
525 polyA (Kwan et al., 2007) were cloned into a Tol2 vector pDestTol2CG2 carrying
526 cmcl2:GFP to drive expression of GFP in the heart. The final plasmid was co-injected
527 with tol2 mRNA into the *Tg(fli1ep:gal4ff)*^{ubs3}*; (UAS:mRFP)* embryos. These mosaic
528 embryos were raised to adulthood and outcrossed with the parental fish line to
529 generate stable fish lines. The resulting *Tg(UAS:EGFPpodxl)* embryos were identified
530 on the basis of GFP expression in the heart; proper apical localization of EGFP-
531 Podocalyxin was confirmed using confocal microscopy. Two transgenic lines, ubs29

532 and ubs30, were isolated, and the ubs29 line showing more homogenous expression
533 levels in endothelium was used in experiments.
534
535 **Immunofluorescence**
536 Immunofluorescence was performed as previously described (Herwig et al., 2011).
537 The following antibodies were used: rabbit anti-zf-Cdh5 1:200 (Blum et al., 2008),
538 rabbit anti-Esama 1:200 (Sauteur et al., 2017), mouse anti-human-Zo-1 1:100
539 (Thermofisher), rabbit anti-Rasip1 1:500 (this paper), chicken anti-GFP 1:200
540 (Abcam), Alexa 405 goat anti-chicken immunoglobulin Y (IgY H&L) 1:1,000 (Abcam),
541 Alexa 568 goat anti-rabbit immunoglobulin G (IgG) 1:1,000, and Alexa 633 goat anti-
542 mouse IgG 1:1,000 (both from Thermofisher). The anti-zf-Rasip1 antibodies were
543 raised in rabbits against a synthetic peptide (CRTFLWGLDQDELPANQRTRL-COOH)
544 comprising the terminal amino acid residues (aa970-989) of the protein (Yenzym,
545 Antibodies LLC, Brisbane (CA, USA)).
546
547 **Live Imaging**
548 Time-lapse imaging was performed as previously described (Paatero et al., 2018). All
549 movies were taken with Leica SP5 or SP8 confocal microscopes using a 40x water
550 immersion objective (NA = 1.1) with a frame size of 1024x512 or 1024x1024 pixels.
551 Routinely, z stacks consisted of 80–100 slices with a step size of 0.8–1 µm. Stacks
552 were taken every 8- or 10-min. High-resolution imaging was performed a Zeiss
553 LSM880 microscope using a 40x water immersion objective (NA = 1.2) using a vertical
554 step size of 0.25 µm.
555
556 **Statistics**

557 Unless explicitly stated, all results shown were obtained from at least 3 independent
558 experiments, sample sizes were not predetermined, the experiments were not
559 randomized and investigators were not blinded to allocation during experiments and
560 outcome assessment. Statistical analyses were performed using Prism software
561 (GraphPad) and ordinary unpaired two-tailed Mann-Whitney test.
562

563 ## Author Contributions

564

565 H.-G.B. and M.A. conceived the project; M.L. performed most experiments and
566 prepared the figures. C.B. generated *rasip1* mutant alleles and performed initial
567 experiments. N.S. characterized *radil-b* mutants; I.P. generated the
568 *Tg(UAS:EGFPpodxl)*^{ubs29} zebrafish line; J.Y. analyzed *heg1* and *ccm1* morphants;
569 C.W.W. and W.Y. provided the anti-zf-Rasip1 antibody; M.A and H.-G.B. supervised
570 the project. M.L., M.A. and H.-G.B. wrote the manuscript. All authors read and
571 approved the manuscript.

572

573 ## Acknowledgements

574

575 We would like to thank the Biozentrum Imaging Core Facility for ceaseless support,
576 Dr. Li-Kun Phng and Gustavo Aguilar for critically reading the manuscript, Dr. Anne
577 Karine Lagendijk and Dr. Benjamin M. Hogan for providing the transgenic VE-cad-
578 Venus reporter , Dr. David Dylus for help on phylotypic analysis and Kumuthini
579 Kulendra and Mattias Thimm for fish husbandry. M.L. was supported by a fellowship
580 from the Werner-Siemens-Foundation (Zug). This work has been supported by the
581 Kantons Basel-Stadt and Basel-Land and by a grant from the Swiss National Science
582 Foundation to M.A.

583

584 # References

585 Adams, R.H., Alitalo, K., 2007. Molecular regulation of angiogenesis and
586 lymphangiogenesis. Nature Reviews Molecular Cell Biology 8, 464–478.
587 doi:10.1038/nrm2183
588 Aleström, P., D'Angelo, L., Midtlyng, P.J., Schorderet, D.F., Schulte-Merker, S.,
589 Sohm, F., Warner, S., 2019. Zebrafish: Housing and husbandry
590 recommendations. Lab Anim 51, 002367721986903–12.
591 doi:10.1177/0023677219869037
592 Ando, K., Fukuhara, S., Izumi, N., Nakajima, H., Fukui, H., Kelsh, R.N., Mochizuki,
593 N., 2016. Clarification of mural cell coverage of vascular endothelial cells by live
594 imaging of zebrafish. Development 143, 1328–1339. doi:10.1242/dev.132654
595 Angulo-Urarte, A., Casado, P., Castillo, S.D., Kobialka, P., Kotini, M.P., Figueiredo,
596 A.M., Castel, P., Rajeeve, V., Guasch, M.M.X., Millán, J., Wiesner, C., Serra, H.,
597 Muixi, L., Casanovas, O., als, F.V.X., Affolter, M., Gerhardt, H., Huveneers, S.,
598 Belting, H.-G., Cutillas, P.R., Graupera, M., 2018. Endothelial cell
599 rearrangements during vascular patterning require PI3-kinase-mediated inhibition
600 of actomyosin contractility. Nature Communications 1–16. doi:10.1038/s41467-
601 018-07172-3
602 Asakawa, K., Kawakami, K., 2008. Targeted gene expression by the Gal4-UAS
603 system in zebrafish. Develop. Growth Differ. 50, 391–399. doi:10.1111/j.1440-
604 169X.2008.01044.x
605 Baeyens, N., Bandyopadhyay, C., Coon, B.G., Yun, S., Schwartz, M.A., 2016.
606 Endothelial fluid shear stress sensing in vascular health and disease. J. Clin.
607 Invest. 126, 821–828. doi:10.1172/JCI83083
608 Barlow, H.R., Cleaver, O., 2019. Building Blood Vessels—One Rho GTPase at a
609 Time. Cells 8, 545–25. doi:10.3390/cells8060545
610 Barry, D.M., Koo, Y., Norden, P.R., Wylie, L.A., Xu, K., Wichaidit, C., Azizoglu, D.B.,
611 Zheng, Y., Cobb, M.H., Davis, G.E., Cleaver, O., 2016. Rasip1-Mediated Rho
612 GTPase Signaling Regulates Blood Vessel Tubulogenesis via Nonmuscle
613 Myosin II. Circ Res 119, 810–826. doi:10.1161/CIRCRESAHA.116.309094
614 Betz, C., Lenard, A., Belting, H.-G., Affolter, M., 2016. Cell behaviors and dynamics
615 during angiogenesis. Development 143, 2249–2260. doi:10.1242/dev.135616
616 Blum, Y., Belting, H.-G., Ellertsdottir, E., Herwig, L., Lüders, F., Affolter, M., 2008.
617 Complex cell rearrangements during intersegmental vessel sprouting and vessel
618 fusion in the zebrafish embryo. Developmental Biology 316, 312–322.
619 doi:10.1016/j.ydbio.2008.01.038
620 Bonello, T.T., Perez-Vale, K.Z., Sumigray, K.D., Peifer, M., 2018. Rap1 acts via
621 multiple mechanisms to position Canoe and adherens junctions and mediate
622 apical-basal polarity establishment. Development 145, dev157941–21.
623 doi:10.1242/dev.157941
624 Bryant, D.M., Datta, A., Rodriguez-Fraticelli, A.E., Peränen, J., Martin-Belmonte, F.,
625 Mostov, K.E., 2010. A molecular network for de novo generation of the apical
626 surface and lumen. Nat Cell Biol 12, 1035–1045. doi:10.1038/ncb2106
627 Choi, W., Acharya, B.R., Peyret, G., Fardin, M.-A., Mège, R.-M., Ladoux, B., Yap,
628 A.S., Fanning, A.S., Peifer, M., 2016. Remodeling the zonula adherens in
629 response to tension and the role of afadin in this response. The Journal of Cell
630 Biology 213, 243–260. doi:10.1083/jcb.201506115
631 Davis, G.E., Stratman, A.N., Sacharidou, A., Koh, W., 2011. Molecular Basis for
632 Endothelial Lumen Formation and Tubulogenesis During Vasculogenesis and

633 Angiogenic Sprouting, 1st ed, International Review Of Cell and Molecular
634 Biology. Elsevier Inc. doi:10.1016/B978-0-12-386041-5.00003-0
635 de Kreuk, B.-J., Gingras, A.R., Knight, J.D., Liu, J.J., Gingras, A.-C., Ginsberg, M.H.,
636 2016. Heart of glass anchors Rasip1 at endothelial cell-cell junctions to support
637 vascular integrity. eLife 5, e11394. doi:10.7554/eLife.11394
638 Duran, C.L., Howell, D.W., Dave, J.M., Smith, R.L., Torrie, M.E., Essner, J.J.,
639 Bayless, K.J., 2017. Molecular Regulation of Sprouting Angiogenesis. Compr
640 Physiol 8, 153–235. doi:10.1002/cphy.c160048
641 Gebala, V., Collins, R., Geudens, I., Phng, L.-K., Gerhardt, H., 2016. Blood flow
642 drives lumen formation by inverse membrane blebbing during angiogenesis
643 in vivo. Nat Cell Biol 18, 443–450. doi:10.1038/ncb3320
644 Gingras, A.R., Liu, J.J., Ginsberg, M.H., 2012. Structural basis of the junctional
645 anchorage of the cerebral cavernous malformations complex. The Journal of Cell
646 Biology 199, 39–48. doi:10.1083/jcb.201205109
647 Gingras, A.R., Puzon-McLaughlin, W., Bobkov, A.A., Ginsberg, M.H., 2016.
648 Structural Basis of Dimeric Rasip1 RA Domain Recognition of the Ras Subfamily
649 of GTP-Binding Proteins. Structure/Folding and Design 24, 2152–2162.
650 doi:10.1016/j.str.2016.10.001
651 Herwig, L., Blum, Y., Krudewig, A., Ellertsdottir, E., Lenard, A., Belting, H.-G.,
652 Affolter, M., 2011. Distinct Cellular Mechanisms of Blood Vessel Fusion in the
653 Zebrafish Embryo. Current Biology 21, 1942–1948.
654 doi:10.1016/j.cub.2011.10.016
655 Hogan, B.M., Bussmann, J., Wolburg, H., Schulte-Merker, S., 2008. ccm1 cell
656 autonomously regulates endothelial cellular morphogenesis and vascular
657 tubulogenesis in zebrafish. Human Molecular Genetics 17, 2424–2432.
658 doi:10.1093/hmg/ddn142
659 Jin, S.W., 2005. Cellular and molecular analyses of vascular tube and lumen
660 formation in zebrafish. Development 132, 5199–5209. doi:10.1242/dev.02087
661 Kleaveland, B., Zheng, X., Liu, J.J., Blum, Y., Tung, J.J., Zou, Z., Sweeney, S.M.,
662 Chen, M., Guo, L., Lu, M.-M., Zhou, D., Kitajewski, J., Affolter, M., Ginsberg,
663 M.H., Kahn, M.L., 2009. Regulation of cardiovascular development and integrity
664 by the heart of glass–cerebral cavernous malformation protein pathway. Nature
665 Medicine 15, 169–176. doi:10.1038/nm.1918
666 Koo, Y., Barry, D.M., Xu, K., Tanigaki, K., Davis, G.E., Mineo, C., Cleaver, O., 2016.
667 Rasip1 is essential to blood vessel stability and angiogenic blood vessel growth.
668 Angiogenesis 1–18. doi:10.1007/s10456-016-9498-5
669 Kwan, K.M., Fujimoto, E., Grabher, C., Mangum, B.D., Hardy, M.E., Campbell, D.S.,
670 Parant, J.M., Yost, H.J., Kanki, J.P., Chien, C.-B., 2007. The Tol2kit: A multisite
671 gateway-based construction kit forTol2 transposon transgenesis constructs. Dev.
672 Dyn. 236, 3088–3099. doi:10.1002/dvdy.21343
673 Lagendijk, A.K., Gomez, G.A., Baek, S., Hesselson, D., Hughes, W.E., Paterson, S.,
674 Conway, D.E., Belting, H.-G., Affolter, M., Smith, K.A., Schwartz, M.A., Yap,
675 A.S., Hogan, B.M., 2017. Live imaging molecular changes in junctional tension
676 upon VE-cadherin in zebrafish. Nature Communications 1–12.
677 doi:10.1038/s41467-017-01325-6
678 Lampugnani, M.G., Dejana, E., Giampietro, C., 2017. Vascular Endothelial (VE)-
679 Cadherin, Endothelial Adherens Junctions, and Vascular Disease (2017). Cold
680 Spring Harbor Perspectives in Biology 9. doi:10.1101/cshperspect.a033720

681 Lawson, N.D., Weinstein, B.M., 2002. In Vivo Imaging of Embryonic Vascular
682 Development Using Transgenic Zebrafish. Developmental Biology 248, 307–318.
683 doi:10.1006/dbio.2002.0711
684 Lenard, A., Ellertsdottir, E., Herwig, L., Krudewig, A., Sauteur, L., Belting, H.-G.,
685 Affolter, M., 2013. In vivo analysis reveals a highly stereotypic morphogenetic
686 pathway of vascular anastomosis. Developmental Cell 25, 492–506.
687 doi:10.1016/j.devcel.2013.05.010
688 Liu, X., Gu, X., Ma, W., Oxendine, M., Gil, H.J., Davis, G.E., Cleaver, O., Oliver, G.,
689 2018. Rasip1 controls lymphatic vessel lumen maintenance by regulating
690 endothelial cell junctions. Development 145. doi:10.1242/dev.165092
691 Mably, J.D., 2006. santa and valentine pattern concentric growth of cardiac
692 myocardium in the zebrafish. Development 133, 3139–3146.
693 doi:10.1242/dev.02469
694 Mably, J.D., Burns, C.G., Chen, J.-N., Fishman, M.C., Mohideen, M.-A.P.K., 2003.
695 heart of glass Regulates the Concentric Growth of the Heart in Zebrafish. Current
696 Biology 13, 2138–2147. doi:10.1016/j.cub.2003.11.055
697 Navis, A., Marjoram, L., Bagnat, M., 2013. Cftr controls lumen expansion and
698 function of Kupffer's vesicle in zebrafish. Development 140, 1703–1712.
699 doi:10.1242/dev.091819
700 Paatero, I., Sauteur, L., Lee, M., Lagendijk, A.K., Heutschi, D., Wiesner, C.,
701 Guzmán, C., Bieli, D., Hogan, B.M., Affolter, M., Belting, H.-G., 2018. Junction-
702 based lamellipodia drive endothelial cell rearrangements in vivo via a VE-
703 cadherin-F-actin based oscillatory cell-cell interaction. Nature Communications
704 1–13. doi:10.1038/s41467-018-05851-9
705 Pannekoek, W.-J., Post, A., Bos, J.L., 2014. Rap1 signaling in endothelial barrier
706 control. Cell Adhesion & Migration 8, 100–107. doi:10.4161/cam.27352
707 Phng, L.-K., Gebala, V., Bentley, K., Philippides, A., Wacker, A., Mathivet, T.,
708 Sauteur, L., Stanchi, F., Belting, H.-G., Affolter, M., Gerhardt, H., 2015. Formin-
709 Mediated Actin Polymerization at Endothelial Junctions Is Required for Vessel
710 Lumen Formation and Stabilization. DEVCEL 32, 123–132.
711 doi:10.1016/j.devcel.2014.11.017
712 Post, A., Pannekoek, W.-J., Ross, S.H., Verlaan, I., Brouwer, P.M., Bos, J.L., 2013.
713 Rasip1 mediates Rap1 regulation of Rho in endothelial barrier function through
714 ArhGAP29. Proc. Natl. Acad. Sci. U.S.A. 110, 11427–11432.
715 doi:10.1073/pnas.1306595110
716 Post, A., Pannekoek, W.J., Ponsioen, B., Vliem, M.J., Bos, J.L., 2015. Rap1 Spatially
717 Controls ArhGAP29 To Inhibit Rho Signaling during Endothelial Barrier
718 Regulation. Molecular and Cellular Biology 35, 2495–2502.
719 doi:10.1128/MCB.01453-14
720 Sauteur, L., Affolter, M., Belting, H.-G., 2017. Distinct and redundant functions of
721 Esama and VE-cadherin during vascular morphogenesis. Development 144,
722 1554–1565. doi:10.1242/dev.140038
723 Sauteur, L., Krudewig, A., Herwig, L., Ehrenfeuchter, N., Lenard, A., Affolter, M.,
724 Belting, H.-G., 2014. Cdh5/VE-cadherin Promotes Endothelial Cell Interface
725 Elongation via Cortical Actin Polymerization during Angiogenic Sprouting.
726 CellReports 9, 504–513. doi:10.1016/j.celrep.2014.09.024
727 Stainier, D.Y., Fouquet, B., Chen, J.N., Warren, K.S., Weinstein, B.M., Meiler, S.E.,
728 Mohideen, M.A., Neuhauss, S.C., Solnica-Krezel, L., Schier, A.F., Zwartkruis, F.,
729 Stemple, D.L., Malicki, J., Driever, W., Fishman, M.C., 1996. Mutations affecting

730 the formation and function of the cardiovascular system in the zebrafish embryo.
731 Development 123, 285–292.
732 StriliC, B., KuCera, T., Eglinger, J., Hughes, M.R., McNagny, K.M., Tsukita, S.,
733 Dejana, E., Ferrara, N., Lammert, E., 2009. The Molecular Basis of Vascular
734 Lumen Formation in the Developing Mouse Aorta. DEVCEL 17, 505–515.
735 doi:10.1016/j.devcel.2009.08.011
736 Traver, D., Paw, B.H., Poss, K.D., Penberthy, W.T., Lin, S., Zon, L.I., 2003.
737 Transplantation and in vivo imaging of multilineage engraftment in zebrafish
738 bloodless mutants. Nat Immunol 4, 1238–1246. doi:10.1038/ni1007
739 Wilson, C.W., Parker, L.H., Hall, C.J., Smyczek, T., Mak, J., Crow, A., Posthuma, G.,
740 De Mazière, A., Sagolla, M., Chalouni, C., Vitorino, P., Roose-Girma, M.,
741 Warming, S., Klumperman, J., Crosier, P.S., Ye, W., 2013. Rasip1 regulates
742 vertebrate vascular endothelial junction stability through Epac1-Rap1 signaling.
743 Blood 122, 3678–3690. doi:10.1182/blood-2013-02-483156
744 Wilson, C.W., Ye, W., 2014. Regulation of vascular endothelial junction stability and
745 remodeling through Rap1-Rasip1 signaling. Cell Adhesion & Migration 8, 76–83.
746 doi:10.4161/cam.28115
747 Xu, K., Chong, D.C., Rankin, S.A., Zorn, A.M., Cleaver, O., 2009. Rasip1 is required
748 for endothelial cell motility, angiogenesis and vessel formation. Developmental
749 Biology 329, 269–279. doi:10.1016/j.ydbio.2009.02.033
750 Xu, K., Sacharidou, A., Fu, S., Chong, D.C., Skaug, B., Chen, Z.J., Davis, G.E.,
751 Cleaver, O., 2011. Blood vessel tubulogenesis requires Rasip1 regulation of
752 GTPase signaling. Developmental Cell 20, 526–539.
753 doi:10.1016/j.devcel.2011.02.010
754

755 # Figure legends

756 **Figure 1: Vascular defects in zebrafish *rasip1* mutants. (a)** Conserved Rasip1
757 protein domains. RA: Ras association domain. FHA forkhead-association domain.
758 DIL: dilute domain. The *rasip1*^{ubs28} mutant allele consists of a 35kb deletion comprising
759 all three domains. **(b)** quantification of cranial hemorrhages in *rasip1*^{ubs28} mutant
760 embryos. p<0.0001 (Fisher's exact test). **(c)** confocal images of cranial hemorrhages
761 in rasip1^{ubs28} embryos (72 hpf). Blood cells are visualized by gata1:dsRed expression.
762 Scale bar, 50 µm . **(d)** bright field image (BF) of wild-type and *rasip1*^{ubs28} embryos
763 showing pericardial edema. Scale bar, 2 mm. **(e)** confocal images of wild-type and
764 *rasip1*^{ubs28} mutants. Mutants show narrower DA and irregular ISV diameters. Scale
765 bar, 50 µm. **(f)** quantification of DA diameters (µm) during embryonic development (32
766 to 120 hpf). Mann-Whitney test and error bars indicate standard deviation; significance
767 (ns=not significant, *p < 0.1). (WT 32, 48, 72, 120 hpf: *n*=4, 4, 9, 13 embryos;
768 *rasip1*$^{ubs28/+}$ *n*=5, 12, 19, 33; *rasip1*^{ubs28} *n*=6, 10, 9, 10). **(g)** quantification of ISV
769 diameters (µm) during embryonic development (32 to 120 hpf). Embryos were
770 analyzed by unpaired two-tailed Mann-Whitney test and error bars indicate standard
771 deviation; significance (ns=not significant, *p < 0.1, **p < 0.01, ****p < 0.0001). (WT
772 48, 72, 120 hpf: *n*=37, 94, 70 ISVs; *rasip1*$^{ubs28/+}$ *n*=104, 52, 198; *rasip1*^{ubs28} *n*=67, 38,
773 65).

774

775 **Figure 2: Formation of multicellular vessels is impaired in *rasip1* mutants. (a)**
776 Still pictures of time-lapse movies (s-movies 7 and 8) showing endothelial cell
777 junctions (Cdh5-Venus) in wild-type and *rasip1*^{ubs28} embryos. White arrowheads show
778 maintained junctional in wild-type ISV sprouts. Yellow arrowheads indicate junctional
779 detachment in mutant embryos. Scale bars, 20 µm. Bottom row: closeups of showing

780 junctional detachment in a^4 and a^5. **(b-e)** Quantification of junctional and cellular
781 configuration during ISV formation in wild-type and *rasip1*^{ubs28} mutant embryos. **(b)**
782 Percentage multicellular tubes at 48 hpf (wt *n*=8, mut *n*=6). **(c)** Speed of multicellular
783 tube formation (wt *n*=5, mut *n*=6). **(d)** Percentage of ISV with multicellular configuration
784 per embryo (WT *n*=4, mut *n*=5). **(e)** Percentage of single cell ISVs at 32 hpf (WT *n*=8,
785 mut *n*=8). Quantifications were done by counting ISVs showing the respective
786 phenotypes, averaged by total ISVs analysed per embryo. **(f)** Immunofluorescence of
787 Zo-1 and Esama in *Tg(kdrl:EGFP)*^{s843} at 32 hpf. Schematic drawings on the right show
788 the different cellular configurations of multicellular (wt) and unicellular (*rasip1* mutant)
789 ISVs. Scale bars, 5 µm. The data was analyzed by unpaired two-tailed Mann-Whitney
790 test and error bars indicate standard deviation; significance (*$p < 0.1$, **$p < 0.01$).
791
792 **Figure 3: Requirement of Rasip 1 for dynamic re-localization of junctional**
793 **proteins and junctional ring formation during anastomosis. (a-c)** Still pictures of
794 time-lapse movies (s-movies 9-11) showing normal junctional patch to ring
795 transformation in wild-type (a) and abberant ring formation in *rasip1*^{ubs28} mutants (b,
796 c). Transgenic embryos expressing a VE-cadherin-Venus fusion protein were imaged,
797 starting at 30 hpf. Scale bar, 5 µm. **(d)** Immunofluorescence analysis of Zo-1 and VE-
798 cadherin in *Tg(kdrl:EGFP)*^{s843} at 32 hpf. *rasip1*^{ubs28} mutants show reticulated junctions
799 between two cells in the DLAV; wild-type embryo forms a cleared, ring-shaped
800 junction. Scale bars, 20 µm (overview) and 5 µm (inset). **(e)** Immunofluorescence
801 analysis of Zo-1 and ESAMa in *Tg(kdrl:EGFP)*^{s843} at 32 hpf showing a collapsed
802 junctional ring in *rasip 1*^{ubs28} mutants . Scale bars, 5 µm. **(f)** Quantification of observed
803 junctional phenotypes at 32 hpf. *rasip1*^{ubs28} mutants show significant number of

804 reticulated junctions and collapsed anastomotic rings compared to wild-type (WT *n*=6
805 embryos, 53 analyzed rings, mut *n*=8, 68, Chi-Square: p<0.0001.
806
807 **Figure 4: Protracted delays in lumen formation in *rasip1* mutants. (a, b)** Live
808 images of *Tg(kdrl:EGFP)*^{s843}*; (gata1a:DsRed)*^{sd2} embryos. **(a)** Still images of a time-
809 lapse movies (s-movies 14, 15) starting at 30 hpf. **(b)** Tracking of individual
810 unlumenized ISV during embryonic development (32 to 96 hpf). Scale bars, 20 µm.
811 **(c)** Percentage of blood carrying ISVs at 96 hpf (WT *n*=3 embryos, 28 analyzed ISVs,
812 mut *n*=5, 46). Analyzed by unpaired two-tailed Mann-Whitney test and error bars
813 indicate standard deviation; significance (*p < 0.1).
814
815 **Figure 5: Analysis of ectopic luminal pockets during DLAV formation in *rasip1***
816 **mutants. (a)** Still pictures of time-lapse movies (s-mov 16, 17) showing for the
817 emergence of ectopic luminal pockets (yellow arrowheads) in *rasip1* mutants. **(b)**
818 Schematic representation of possible cellular localization of ectopic lumens. To
819 differentiate between these possibilities two types of experiments: microangiography
820 (c) and colocalization of luminal pockets with junctional marker (d). **(c)** Visualization of
821 ectopic lumens and patent lumens in a *rasip1*^{ubs28} embryo (36 hpf). Ectopic luminal
822 pockets are indirectly visualized by the absence of cytoplasmic EGFP (yellow
823 arrowhead) (*Tg(kdrl:EGFP)*^{s843}). The patent lumen is marked by microangiography
824 using quantum dots in red (third panel in black). Ectopic lumens are not part of the
825 patent vasculature. **(d)** Still pictures of time-lapse movie (s-mov 18-21) during lumen
826 formation in the DLAV from around 32 hpf onward in wild-type (top) and *rasip1*^{ubs28}
827 (bottom) embryos. Endothelial cells are labeled with mRFP (greyscale images),

828 junctions are labeled by VE-cad-Venus (merged images). Yellow arrowheads indicate
829 the ectopic luminal pockets in a *rasip1* mutant. Scale bar, 5 µm.
830
831 **Figure 6: Apical to junctional re-localization of Rasip1 during blood vessel**
832 **fusion. (a-c)** Immunofluorescent labeling of Rasip1 and VE-cadherin during different
833 stages of DLAV formation (30 to 36 hpf). At 32hpf, Rasip1 is restricted to the apical
834 surface of the anastomotic ring (yellow arrowheads). At 36hpf, Rasip1 localizes to
835 endothelial junctions (VE-cadherin, white arrowheads). Scale bars, 20 µm (overview)
836 and 5 µm (inset).
837
838
839 **Figure 7: Phenotypic comparison *of radil-b* single and of *rasip1/radil-b* double**
840 **mutants suggests partially overlapping functions during vascular**
841 **morphogenesis. (a)** Immunofluorescence analysis of Zo-1 and VE-cadherin
842 distribution in *Tg(kdrl:EGFP)*^{s843} at 32 hpf. **(b)** Live images at 48 hpf using *Tg(ve-*
843 *cad:ve-cadVENUS); Tg(fliep:gal4ff)*^{ubs3}*; (UAS:mRFP*) reporter lines. Scale bars: 20
844 µm
845
846 **Figure 8: Loss of Ccm1 and Heg1 phenocopies aspects of *rasip1* mutants. (a)**
847 Live images of Tg(kdrl:EGFP)^{s843}; (gata1:Dsred)^{sd2} at 72 hpf. *ccm1* and *heg1*
848 morphants display mesenphalic hemorrhages while cranial circulation appears
849 completely disrupted. In addition, the MsV (Mesencephalic veins) and DLV (dorsal
850 longitudinal vein) (yellow arrowheads) are malformed. Scale bar, 50 µm. **(b)** Live
851 images of control, *ccm1* and *heg1* morphants at 32 hpf. *ccm1* and *heg1* morphants
852 show reduced DA diameters and defective ISV formation. Scale bar, 20 µm. **(c)**

853 Immunofluorescence analysis of control, *Ccm1* and *Heg1* morphants at 32 hpf.
854 Transgenic *Tg(kdrl:EGFP)*^{s843} embryos were stained for VE-cadherin. Scale bar, 5 µm.
855 **(d)** Quantification of multicellular ISVs at 48 hpf (Control MO injected embryos *n*=5,
856 24 analyzed ISVs; *Ccm1* MO *n*=4, 26; *Heg1* MO *n*=5, 23). Analyzed by unpaired two-
857 tailed Mann-Whitney test and error bars indicate standard deviation; significance (**p
858 < 0.01).

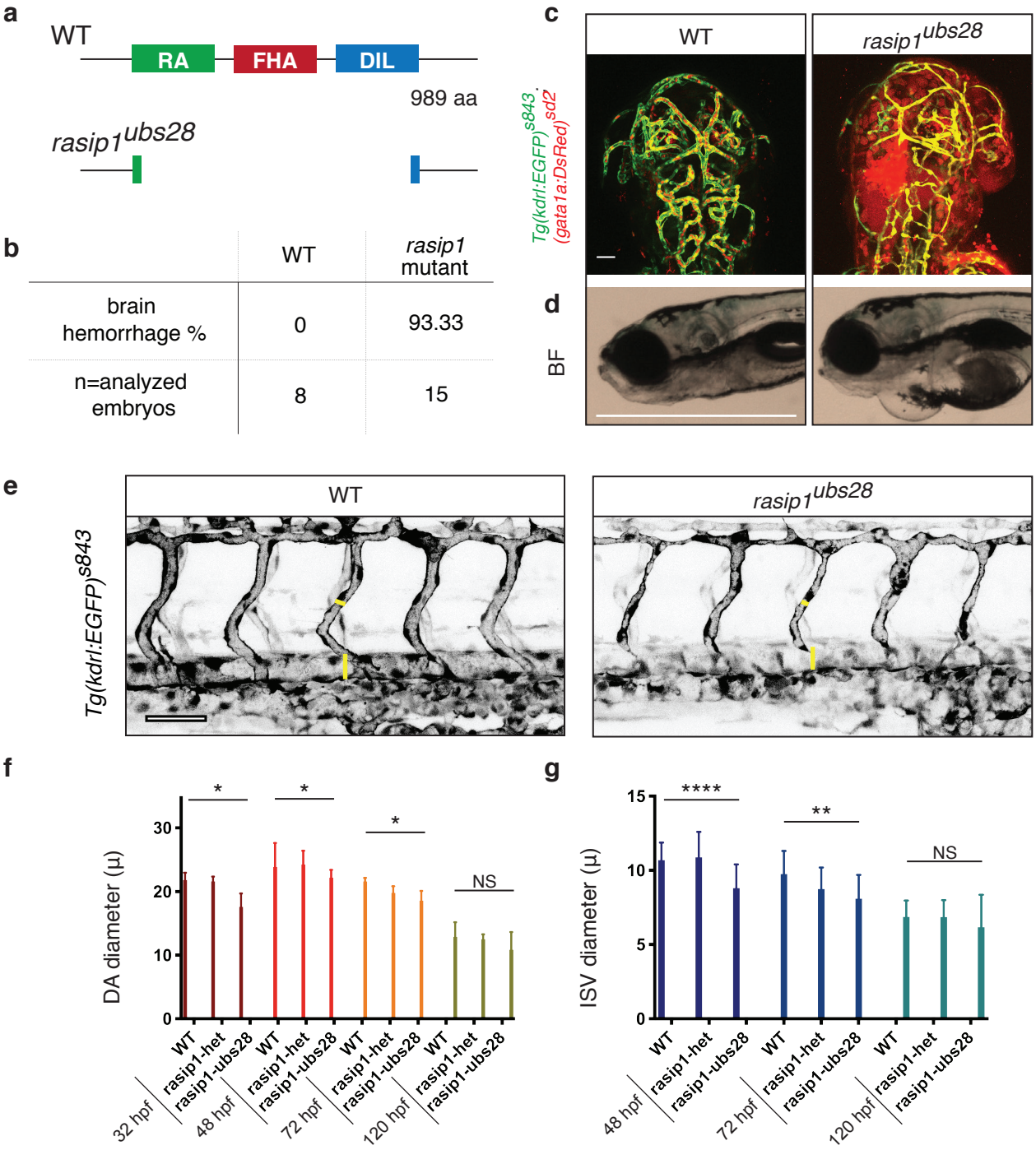
a
WT
RA
FHA
DIL
989 aa
rasip1ubs28
b
WT
rasip1 mutant
brain hemorrhage %
0
93.33
n=analyzed embryos
8
15
c
WT
rasip1ubs28
Tg(kdrl:EGFP)s843, (gata1a:DsRed)sd2
d
BF
e
WT
rasip1ubs28
Tg(kdrl:EGFP)s843
f
DA diameter (µ)
*
*
*
NS
WT
rasip1-het
rasip1-ubs28
32 hpf
48 hpf
72 hpf
120 hpf
g
ISV diameter (µ)
****
**
NS
48 hpf
72 hpf
120 hpf

Figure 1

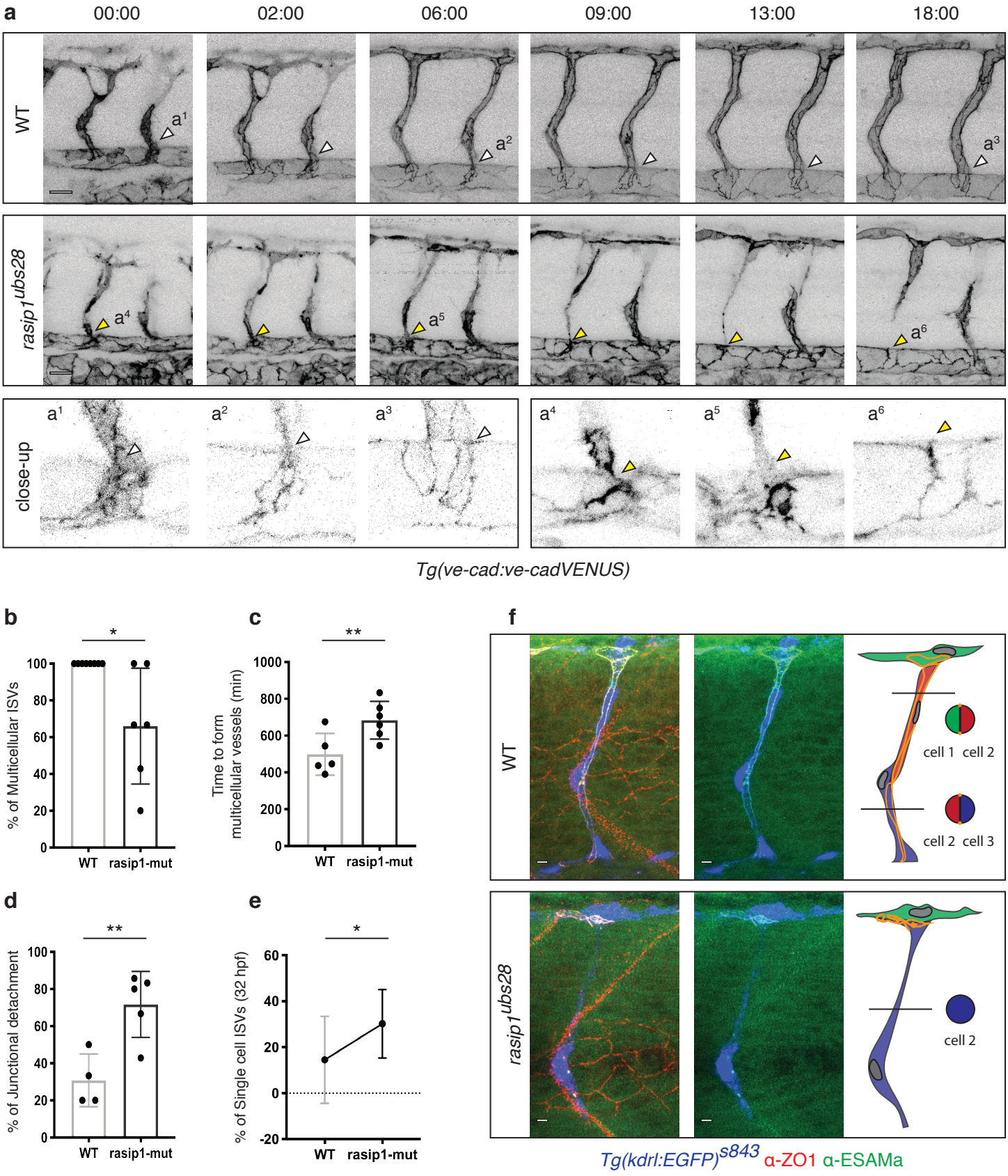
a
00:00
02:00
06:00
09:00
13:00
18:00
WT
rasip1ubs28
close-up
Tg(ve-cad:ve-cadVENUS)
b
% of Multicellular ISVs
WT
rasip1-mut
c
Time to form multicellular vessels (min)
d
% of Junctional detachment
e
% of Single cell ISVs (32 hpf)
f
cell 1
cell 2
cell 3
Tg(kdrl:EGFP)s843 α-ZO1 α-ESAMa

Figure 2

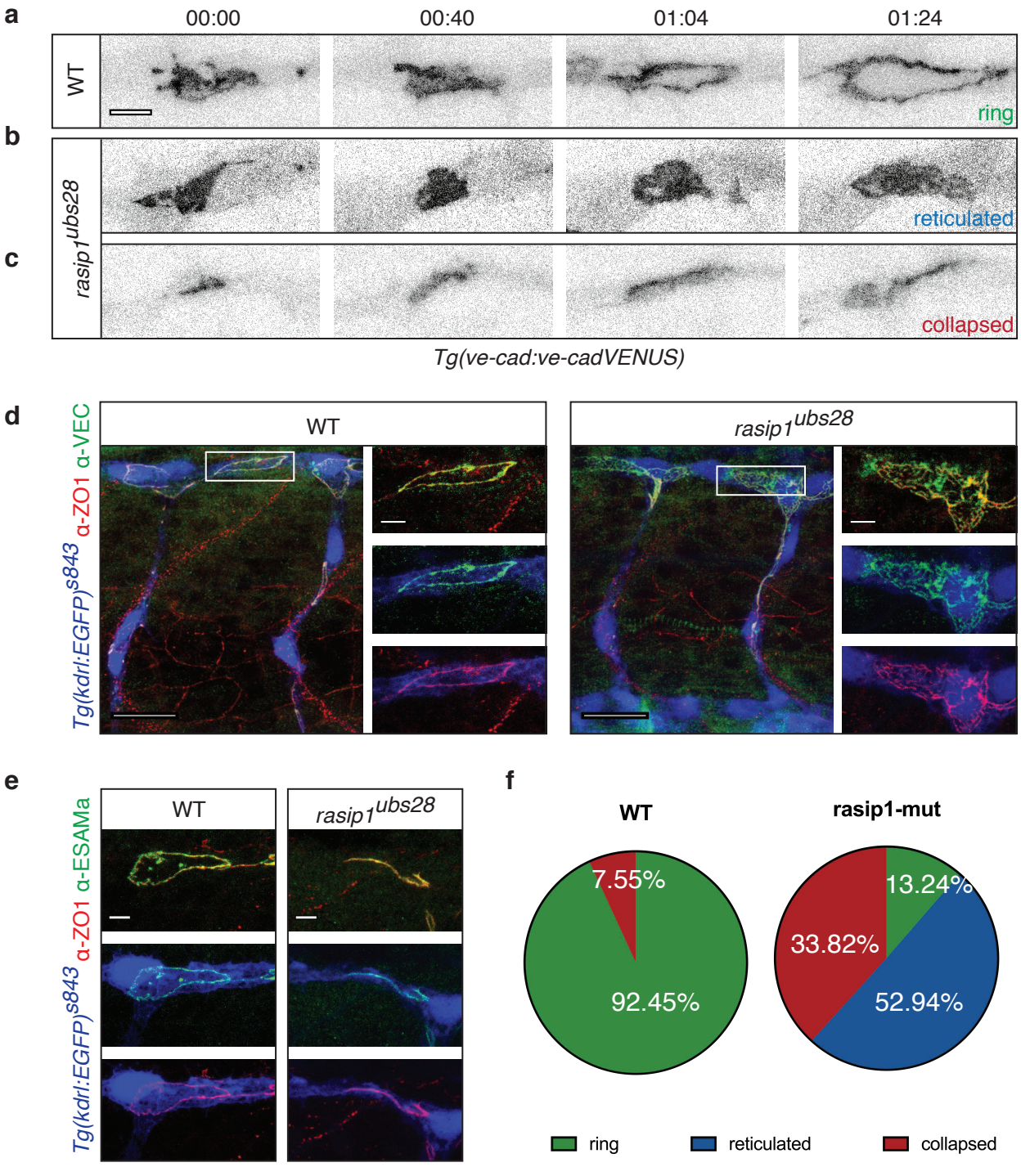
a
00:00
00:40
01:04
01:24
WT
ring
b
rasip1ubs28
reticulated
c
collapsed
Tg(ve-cad:ve-cadVENUS)
d
WT
rasip1ubs28
α-VEC
α-ZO1
Tg(kdrl:EGFP)s843
e
WT
rasip1ubs28
α-ESAMa
α-ZO1
Tg(kdrl:EGFP)s843
f
WT
rasip1-mut
7.55%
92.45%
13.24%
33.82%
52.94%
ring
reticulated
collapsed

Figure 3

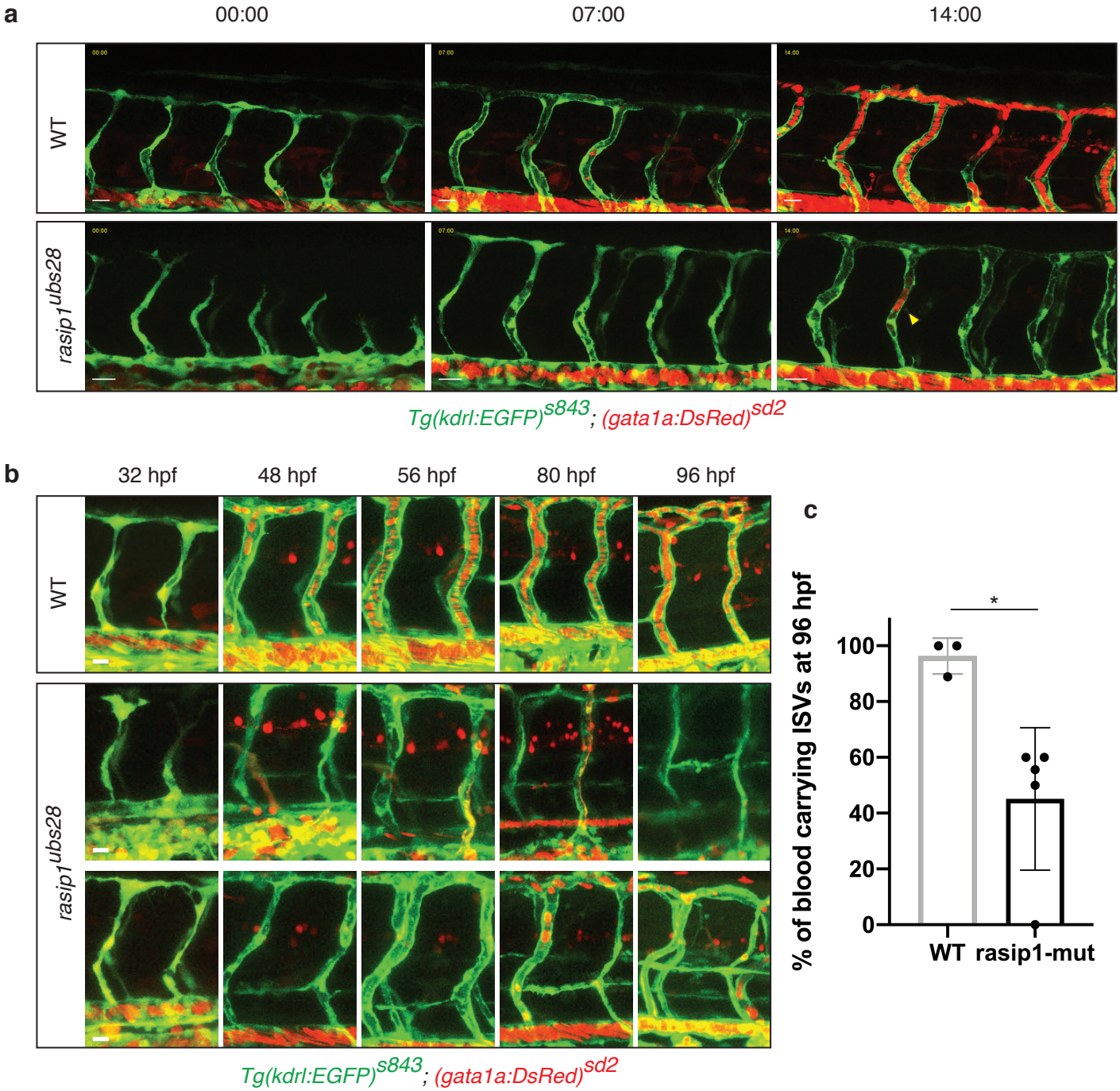
a
00:00
07:00
14:00
WT
rasip1ubs28
Tg(kdrl:EGFP)s843; (gata1a:DsRed)sd2
b
32 hpf
48 hpf
56 hpf
80 hpf
96 hpf
WT
rasip1ubs28
Tg(kdrl:EGFP)s843; (gata1a:DsRed)sd2
c
% of blood carrying ISVs at 96 hpf
100
80
60
40
20
0
*
WT
rasip1-mut

Figure 4

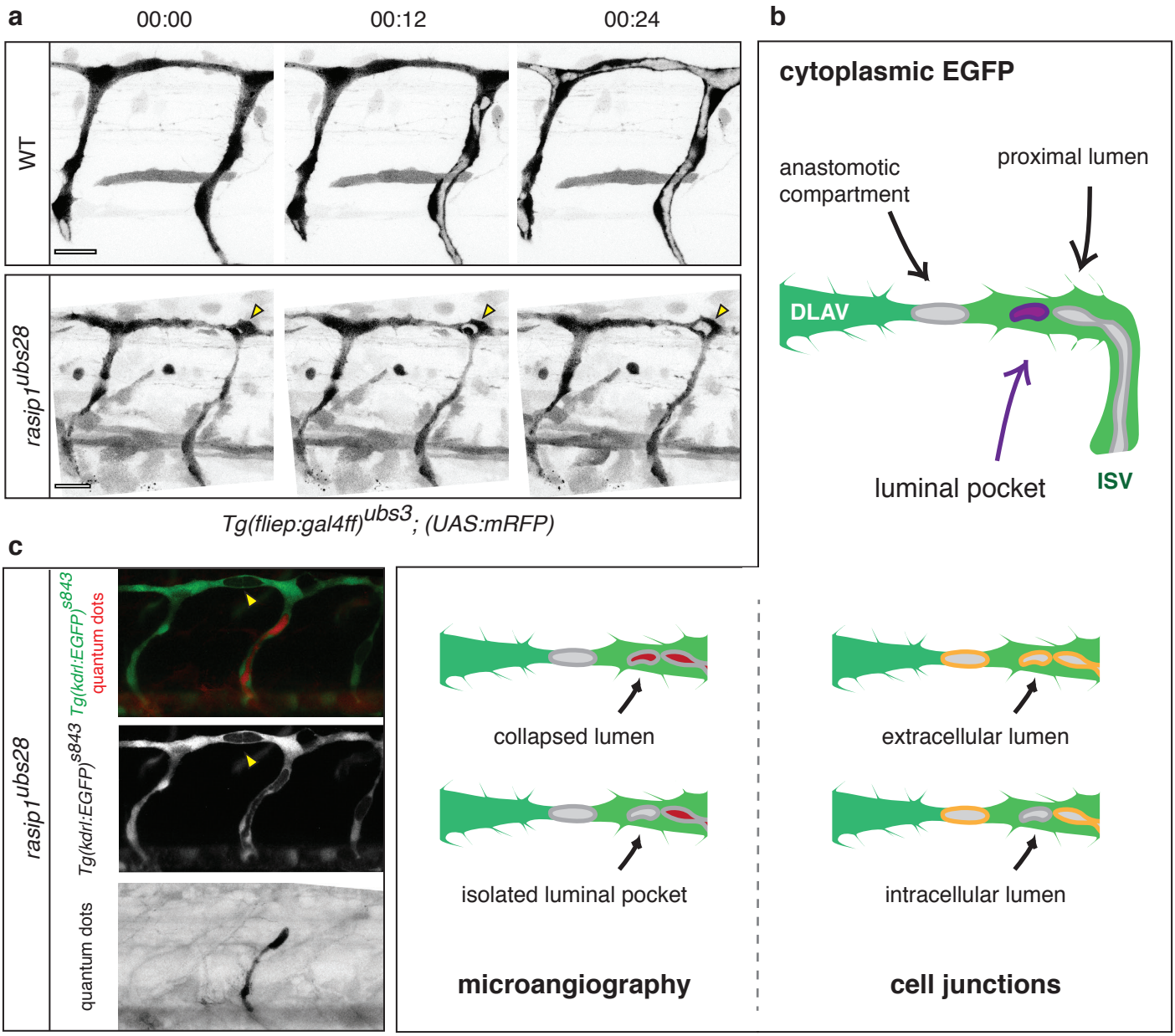
a
00:00
00:12
00:24
WT
rasip1ubs28
Tg(fliep:gal4ff)ubs3; (UAS:mRFP)
b
cytoplasmic EGFP
anastomotic compartment
proximal lumen
DLAV
luminal pocket
ISV
c
rasip1ubs28
Tg(kdrl:EGFP)s843
quantum dots
Tg(kdrl:EGFP)s843
quantum dots
collapsed lumen
isolated luminal pocket
microangiography
extracellular lumen
intracellular lumen
cell junctions

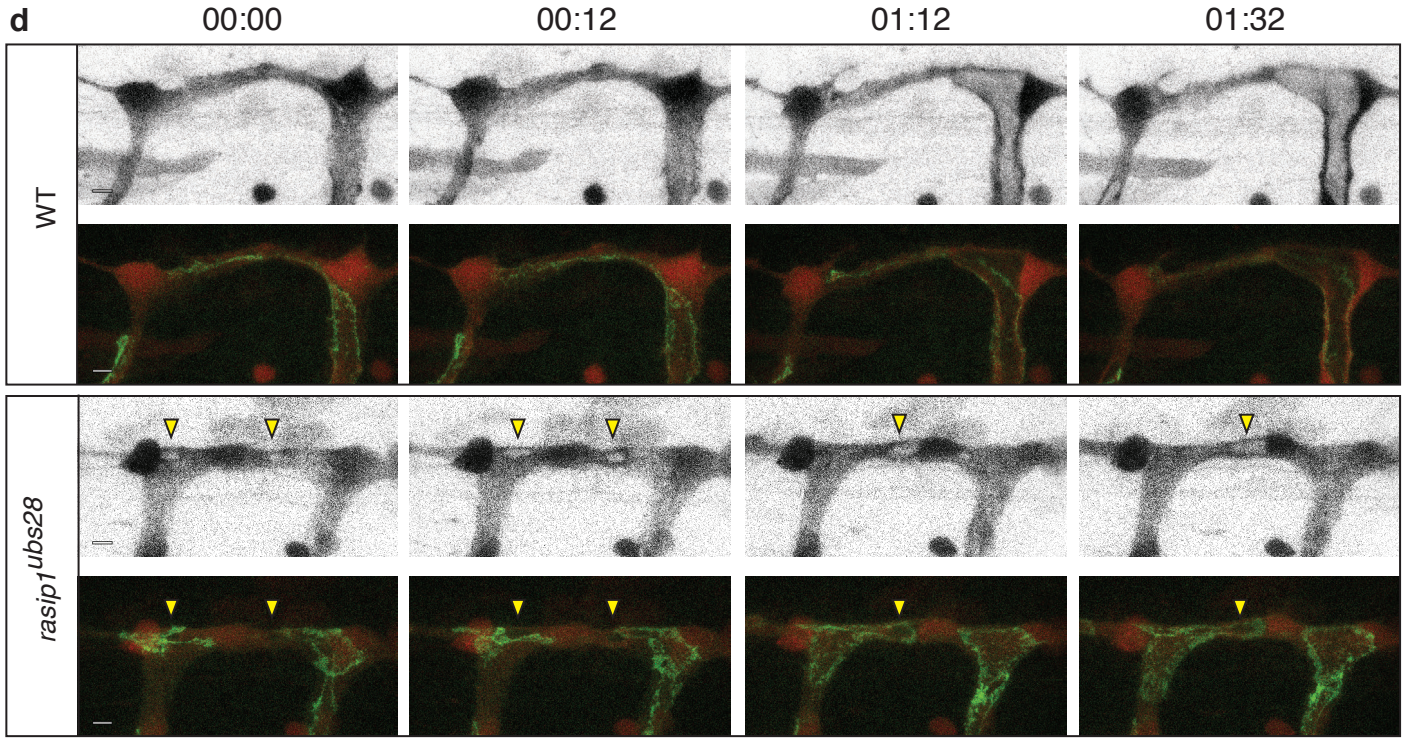
d
00:00
00:12
01:12
01:32
WT
rasip1ubs28
Tg(ve-cad:ve-cadVENUS); Tg(fliep:gal4ff)ubs3; (UAS:mRFP)

Figure 5

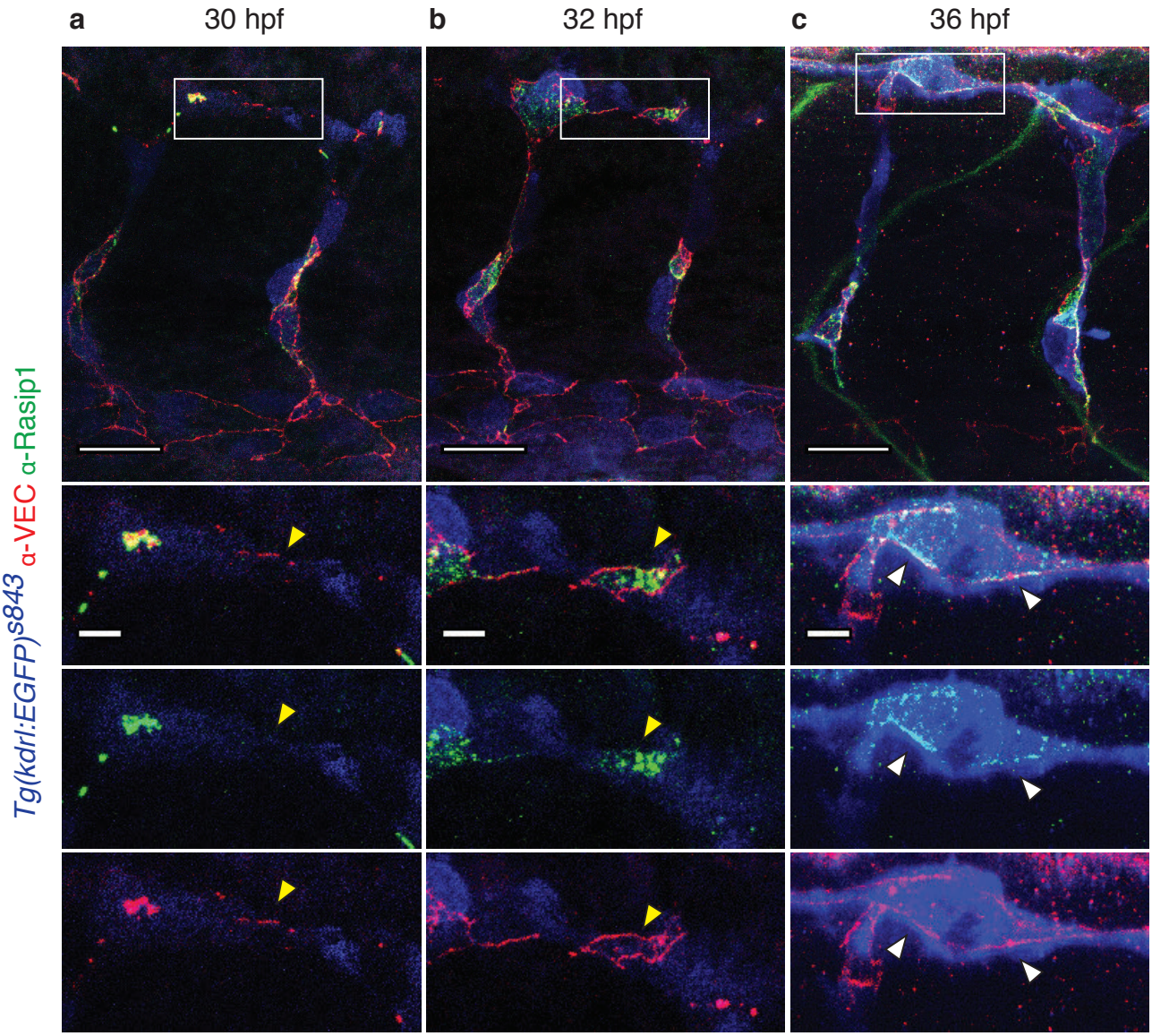

Figure 6

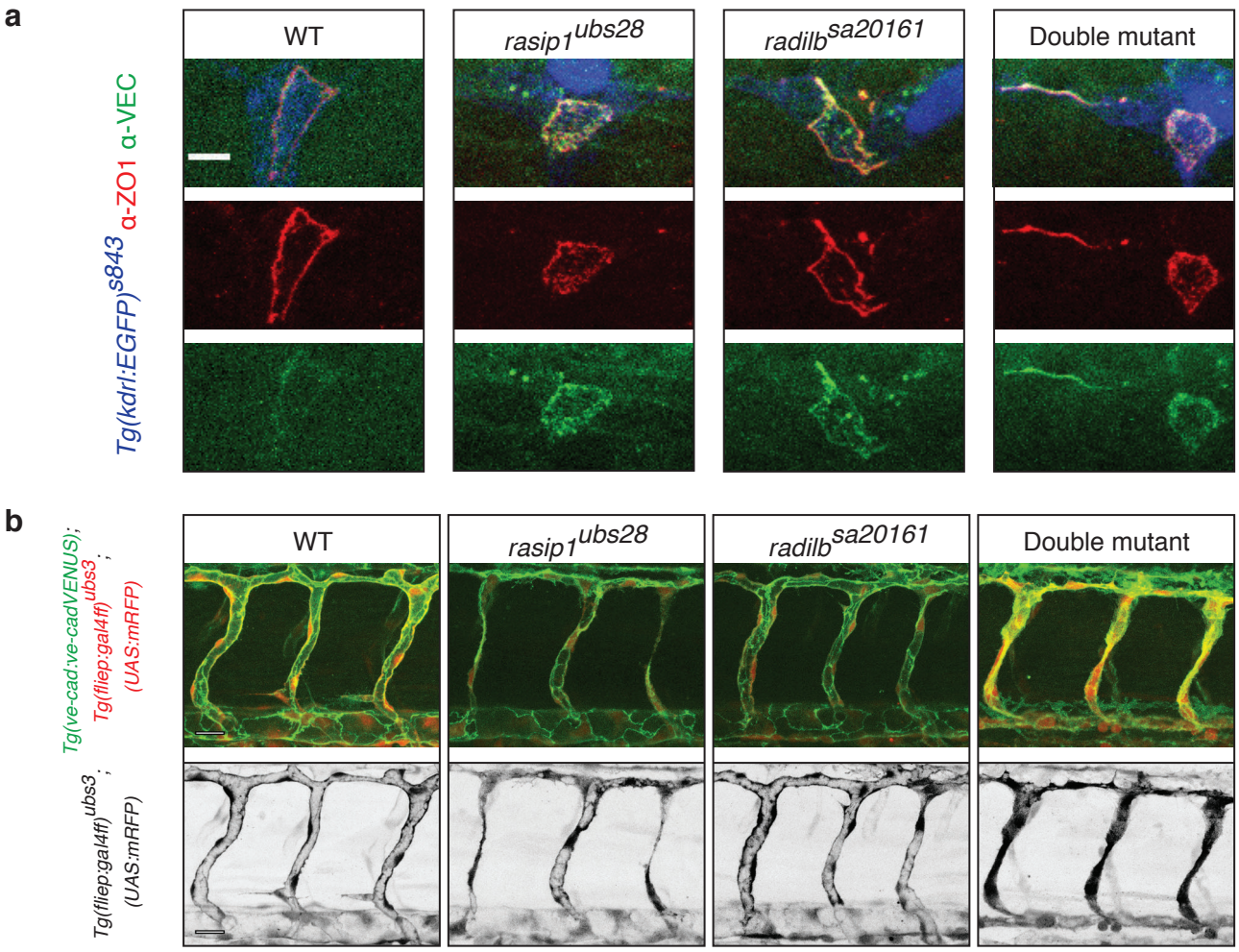
a
WT
rasip1ubs28
radilbsa20161
Double mutant
Tg(kdrl:EGFP)s843 α-ZO1 α-VEC
b
WT
rasip1ubs28
radilbsa20161
Double mutant
Tg(ve-cad:ve-cadVENUS); Tg(fliep:gal4ff)ubs3; (UAS:mRFP)
Tg(fliep:gal4ff)ubs3; (UAS:mRFP)

Figure 7

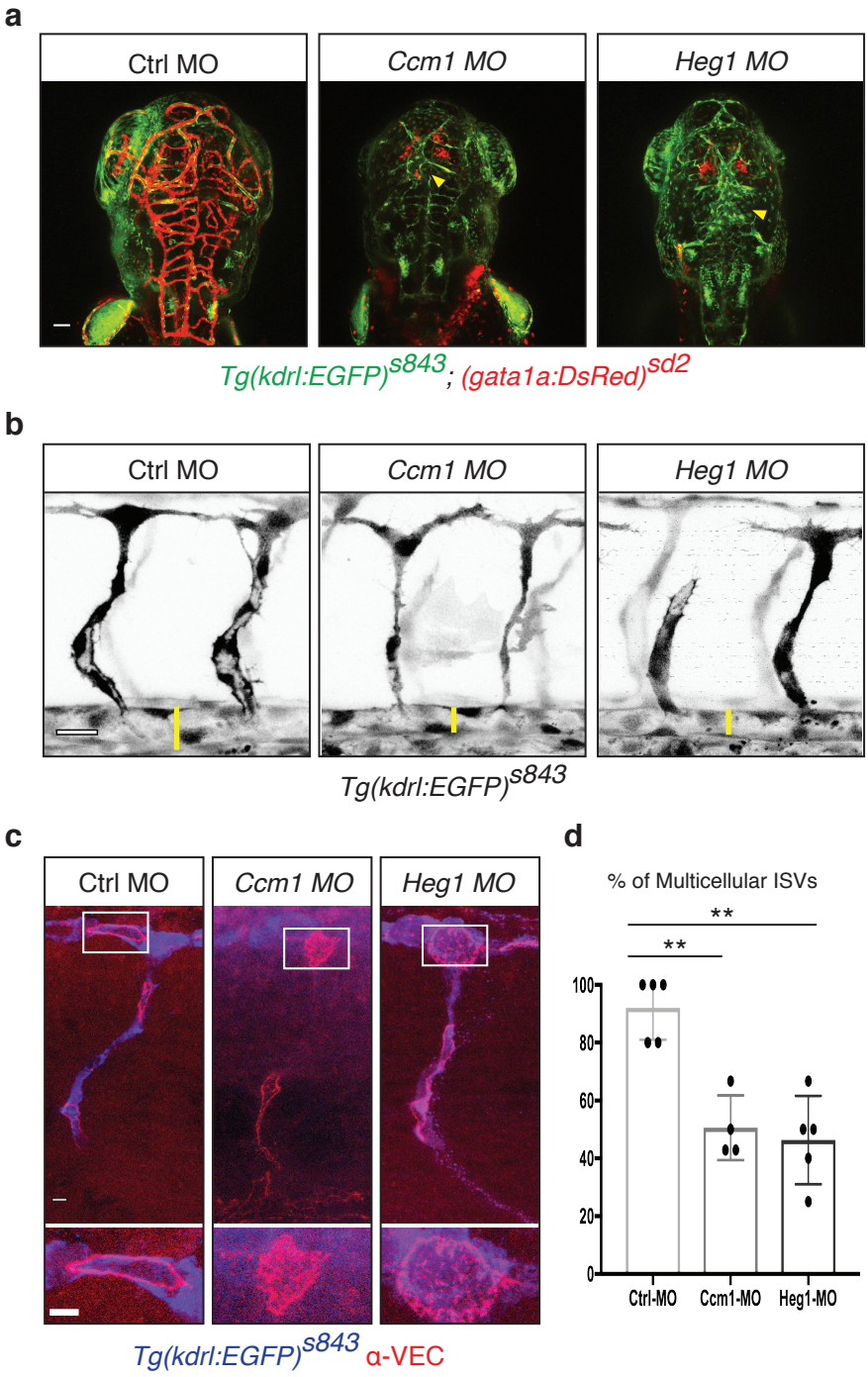
a
Ctrl MO
Ccm1 MO
Heg1 MO
Tg(kdrl:EGFP)s843; (gata1a:DsRed)sd2
b
Ctrl MO
Ccm1 MO
Heg1 MO
Tg(kdrl:EGFP)s843
c
Ctrl MO
Ccm1 MO
Heg1 MO
Tg(kdrl:EGFP)s843 α-VEC
d
% of Multicellular ISVs
**
**
100
80
60
40
20
0
Ctrl-MO
Ccm1-MO
Heg1-MO

Figure 8